

Measuring Water Content of Martian Soil Simulants using Planar Four-Probes

M. G. Buehler¹ martin.g.buehler@jpl.nasa.gov (818-354-4368), T. A. Sant², E. Brizendine², D. Keymeulen¹, G. M. Kuhlman¹, M. G. Schaap³, S. Seshadri¹, and R. C. Anderson¹

¹Jet Propulsion Laboratory, California Institute of Technology, 4800 Oak Grove Drive, Pasadena, CA 91109

²University of Nevada, Reno, ³University of California, Riverside

Abstract^{1,2}—A miniature four-point probe instrument has been developed and applied to the characterization of the moisture content of the Martian soil simulants using fine and coarse silica sand and Moses Lake basalt. The results indicate that the soil resistivity varies over four orders of magnitude as the moisture content varied from 0.1% to over 10%. In addition it was found that forcing too much current through the sand sample resulted in a curious breakdown in the current-voltage characteristic.

TABLE OF CONTENTS

1	INTRODUCTION	1
2	APPARATUS.....	1
2.1	Conductivity Circuitry	2
2.2	Conductivity Waveform.....	3
2.3	Measurement Domain.....	4
3	EXPERIMENTAL PROCEDURES	4
3.1	Waveforms.....	4
3.2	Correlation Coefficient Analysis	6
3.3	Graphical User Interface	6
3.4	Electrode Cleaning Procedure.....	6
4	EXPERIMENTAL RESULTS.....	6
4.1	Sand Sizing	6
4.2	Sand Resistivity	7
5	DATA ANALYSIS.....	8
6	CONCLUSION	8
7	APPENDIX: Conductivity Sensor Calibration	8
8	ACKNOWLEDGMENTS	9
9	REFERENCES	9
10	BIOGRAPHIES	10

1 INTRODUCTION

The moisture content of Martian soils was estimated by the Mars Odyssey, remote sensing Gamma Ray Spectrometer (GRS) to be between 0.25% for the driest part of Mars to 35 ± 15% [1]. This instrument is composed of a GRS and neutron spectrometer. The detection of water is inferred from the hydrogen signal which appears as a 2.2 MeV gamma ray. As this signal increases there is accompanying

decrease in the neutron flux which is absorbed by the hydrogen atoms [2].

The upper limit of 35% is considered to be too large for it is greater than the amount that can be accommodated by alteration of most rock-forming minerals [1] and is typical of water-saturated terrestrial soils. Thus, there is a need to develop instrumentation for direct *in situ* measurement of water in Martian regolith. For this reason, we are in the process of developing such instrumentation. Our goal is to demonstrate the detection of water at less than 1% by weight in simulated Martian regoliths. This paper describes the measurements conducted thus far and suggests extensions of this work to practical instruments that can be used in the field and on the surface of Mars.

2 APPARATUS

The apparatus used in this effort is described in the next few figures. In order to obtain results quickly, we used the E-Tongue 3 apparatus shown in Fig. 1. It was originally designed as an instrument to monitor water quality and biofilm reactions [3]. The sample chamber was re-designed to accommodate the introduction of soil samples into the chamber as seen in Fig. 1a.

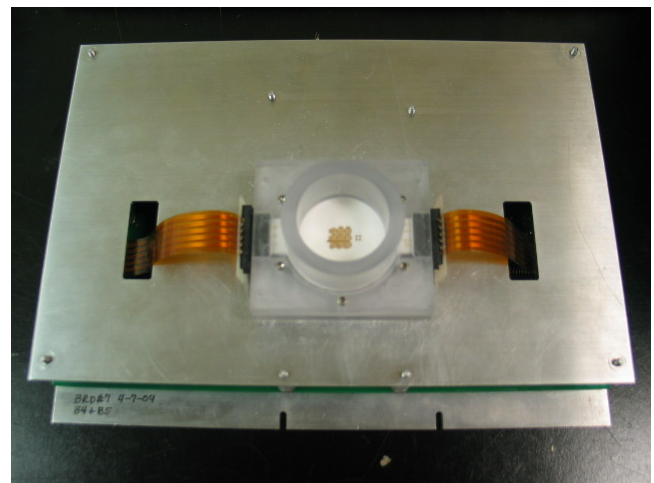


Figure 1a. E-Tongue 3 apparatus showing the new soil sample chamber with sensors at the bottom of the chamber.

¹ 0-7803-8870-4/05/\$20.00 © 2005 IEEE

² Paper Number: 1418/rev3

The sample chamber was fabricated from polycarbonate. It has a 1.2-inch diameter and 0.8-inch depth. As in the original E-Tongue design, the chamber is attached to a ceramic substrate using a dual O-ring seal. The substrates are shown in Fig. 2 and fabricated using hybrid microelectronic fabrication methods where each layer is screen printed onto the ceramic substrate and fired in an air atmosphere at 850°C. The substrate is 1.5-mm thick and is 96% alumina. Electrical contact to the sensors is achieved by using 0.25-mm vias created using laser drilling. The vias are made conducting by screen printing a metal layer that is drawn through the vias using a mild vacuum. The vias are connected to wires screen printed on the underside of the substrate and connected to electrical contacts. The bottom wires are protected by a dielectric layer.

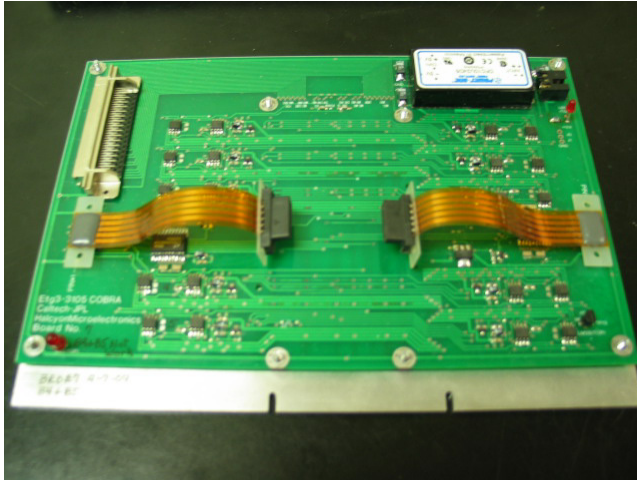


Figure 1b. Electronics board (14.3 cm x 21.7 cm) beneath the top plate showing the flex cables used to connect the electronics to the sensors.

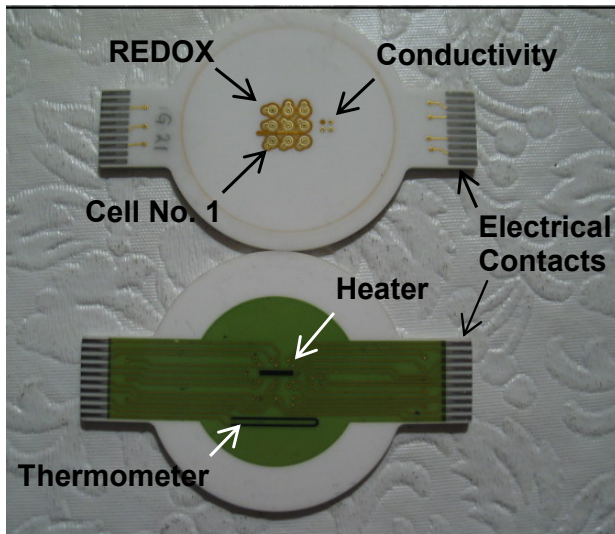


Figure 2. Ceramic substrate with REDOX and conductivity sensors on top and heater and thermometer on bottom. The long dimension is 6.1 cm.

As seen in Fig. 2, the substrate consists of nine REDOX cells and one conductivity sensor. In the experiments

described here, the REDOX cells were biased in an OFF state where no current was allowed to flow either to or from these cells. This was achieved by configuring the REDOX cells in a galvanostat mode and forcing zero current. All electrodes were formed using screen printed gold.

A photomicrograph of the conductivity sensor with gold electrodes is shown in Fig. 3. The probe spacing, s , is 1.25 mm and the diameter, d , of the probes is 0.75 mm. The 0.25-mm diameter laser drilled hole in the ceramic is clearly visible as a dimple in the center of each probe. Each of the probes is given a G-label which corresponds to the labels for the conductivity cell seen in Fig. 4.

2.1 Conductivity Circuitry

The circuitry used to measure the conductivity is shown in Fig. 4. This circuitry is designed as a galvanostat where current is forced through the sensor between two sets of probes (G1 and G4) and the voltage measured between the other two probes (G2 and G3). The conductivity sensor is represented by three resistors shown in the Fig. 4; that is R_{12} , R_{23} , and R_{34} .

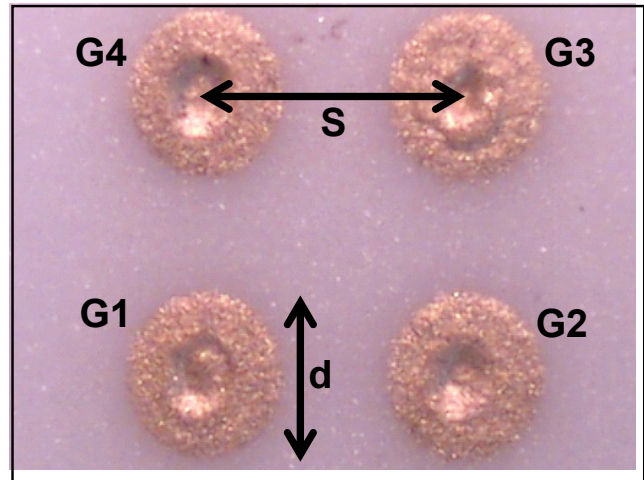


Figure 3. Photomicrograph of gold conductivity sensors' square-array four disc probe where the probe spacing is $s = 1.25$ mm and disc probe diameter is $d = 0.75$ mm.

Current is forced through the sensor by programming the DAC (digital-to-analog converter) seen in the Fig. 4. Thus, current passes through resistor, R_{01} , and then through the conductivity sensor. The sample voltage, V_{01} , is detected by the instrumentation amplifier IA1. The current through the conductivity sensor is given by:

$$I_{01} = V_{01}/R_{01} \quad (1)$$

where $R_{01} = 100$ kohm. For I_{01} in μA and V_{01} in V the operating equation is:

$$I_{01}(\mu A) = 10 \cdot V_{01}(V) \quad (2)$$

The voltage across the sensor, V_{23} , is measured by instrumentation amplifier, IA2. The resistance of the conductivity sensor is given as:

$$R_{23} = (V_{23}/V_{01}) \cdot R_{01} \quad (3)$$

This type of circuit is ratiometric for the measured resistance is a fraction of the resistor R_{01} . Strictly speaking, the determination of the resistance does not require the direct measurement of the current. Thus, the accuracy depends on the ratio of the voltages which are measured by a multiplex ADC using the same reference voltage and the accuracy of R_{01} which is 1%.

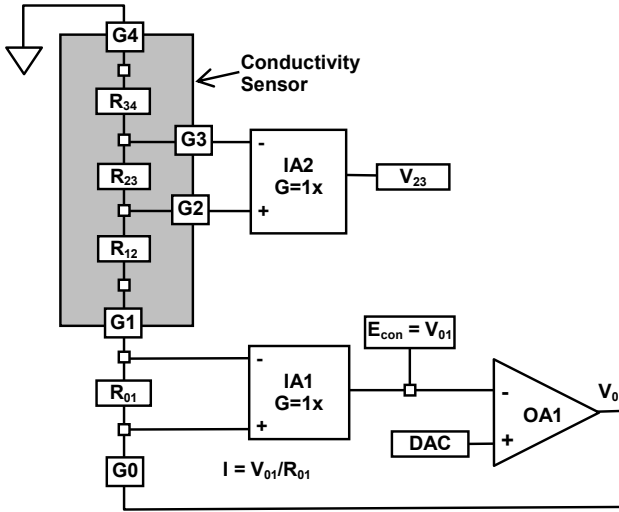


Figure 4. Electronic circuit used to measure soil conductivity. The G-points identify critical nodes in the circuit.

The relationship between the measured resistance, R_{23} , and the sample resistivity, ρ_{∞} , for a semi-infinitely thick sample with a square-array four-point probe, where the probes are far from the edge of the sample, is [4]:

$$\rho_{\infty} = \frac{2\pi \cdot s \cdot R_{23}}{(2 - \sqrt{2})} = G_p \cdot s \cdot R_{23} \quad (4)$$

where G_p is the geometrical factor for the point probes and s is the probe spacing. For the infinitely thick square-array four-point probe, $G_p = 10.726$.

A semi-infinitely thick sample is defined as a sample with a thickness that causes less than a 1% change in G_p . The semi-infinitely thick sample case is satisfied for the square-array four point probe when the sample thickness, t , is more than four times the probe spacing [4]. That is $t_{\infty} > 4 \cdot s$. For $s = 1.25$ mm, the infinitely thick case is determined for $t_{\infty} > 5$ mm. For the sample chamber described above, this can be accommodated by a 10 g sand sample.

The geometrical factor for the disc probes shown in Fig. 3 was determined by measuring the resistivity of various HCl

solutions [5]. The methodology is described in the Appendix. The analysis for the E-Tongue 3 chamber leads to a value for the geometrical factor for the disc probes of $G_d = 24.9$. Thus, the resistivity of the semi-infinitely-thick, square-array four-disc probe with 1.25 mm disc-probe spacing is:

$$\rho_{\infty} (\Omega \cdot \text{cm}) = G_d \cdot s(\text{cm}) \cdot R_{23}(\Omega) = 3.11 \cdot R_{23}(\Omega) \quad (5)$$

This relationship was used to convert the measured resistance, R_{23} , of the sand samples to resistivity.

2.2 Conductivity Waveform

Since conductivity can not be measured using direct current [3] because the electrodes would polarize due to the conducting ions in solution. The E-Tongue 3 waveform is shown in Fig. 5a. This wave was adjusted as seen in Fig. 5b to form a triangle wave current.

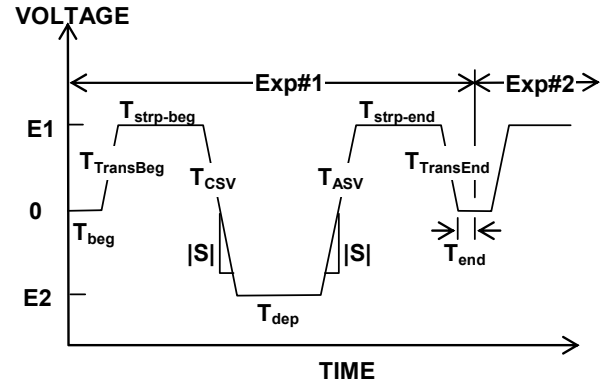


Figure 5a. E-Tongue 3 waveform where the bounds are E_1 and E_2 and the slope is S .

The E-Tongue 3 apparatus is capable of producing the waveform shown in Fig.5a. This waveform was adapted for use with the conductivity sensor and the modified waveform is shown in Fig. 5b. Comparing this waveform with that shown in Fig. 5a, indicates that T_{beg} , $T_{strp-beg}$, T_{dep} , $T_{strp-end}$, T_{end} were set to 0.

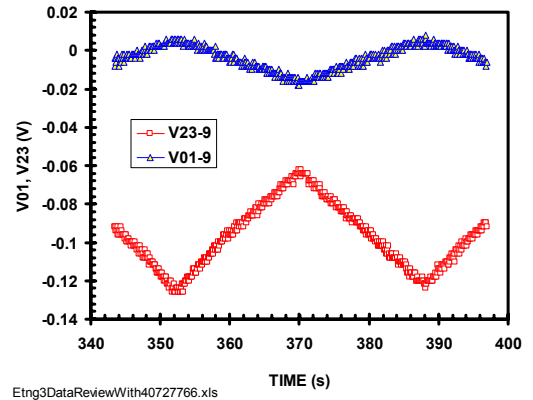


Figure 5b. Conductivity sensor waveform where V_{01} (blue triangles) is the forced voltage and V_{23} (red squares) is the measured voltage.

The frequency of the waves used in this study is in the milli-Hertz range. The waveform shown in Fig. 5b is 40 mHz.

2.3 Measurement Domain

The measurement of conductivity is constrained by equipment limitations. The measurement domain is described in Fig. 6. In this figure, the voltage V_{23} is plotted for R_{23} values with E_{con} as a parameter. The measurement domain for the conductivity sensor is shown as the red dashed area in Fig. 6. The measurement range for this instrument is limited to resistance values that vary from 200 ohms to 50 M ohms.

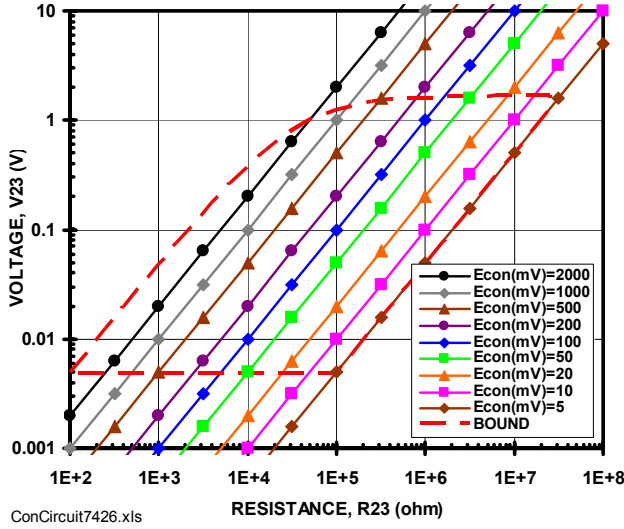


Figure 6. Conductivity sensor measurement domain (red dashed area) for $R_{01} = 100k$ ohm.

The measurement domain results from circuit choices including the R_{01} value (100 kohm) and the resolution of the ADC (analog-to-digital converter) and DAC (digital-to-analog converter). The ADC has a 12-bit resolution and ± 4.096 V range and DAC has a 16-bit resolution and ± 4.096 V range. The ADC's detection resolution is 2 mV/bit. This sets the lower limit for V_{23} at 5 mV. The upper bound for V_{23} is determined by 5 V output capability of the operational amplifier which is $V_0 = 5V$. This results in the following relationship:

$$V_{23} = \frac{R_{23}}{R_{01} (1 + 3 \cdot R_{23}/R_{01})} V_0 \quad (6a)$$

where we have assumed that $R_{12} = R_{23} = R_{34}$. The current through the sample is given by $I_{01} = V_{01}/R_{01}$. For $V_{01} = E_{con}$. The governing equation for the curves in Fig.6 is:

$$V_{23} = (E_{con}/R_{01}) \cdot R_{23} \quad (6b)$$

As seen in the figure, E_{con} values vary from 5 mV to 2 V. Thus setting E_{con} determines the range over which sample resistances can be measured. As seen in the figure, the range for sample resistance varies from 200 ohms to 50 M ohms.

Other factors, that influence the accuracy of the measurements, include over sampling of each measured point and the least squares fitting of many current-voltage points. Depending on the number of additional points, measurements are possible below the bottom of the red-dashed area shown in Fig. 6.

To determine the proper operating conditions, current-voltage data was acquired and its correlation coefficient determined. Data with a correlation coefficient equal to or greater than 0.9 were deemed satisfactory. The details are given in the next section.

3 EXPERIMENTAL PROCEDURES

This section presents the experimental results for two types of sand samples. First the waveforms are described then the experimental results are presented.

3.1 Waveforms

Typical waveform used in these experiments is shown in Fig. 7. During the positive going ramp, 200 data points were acquired and during the negative going ramp an additional 200 points were acquired. Fig. 7a shows the time evolution of the current and voltage signals and Fig. 7b shows the current voltage characteristic. The digitization characteristics of the ADC is clearly evident in these figures as the stair-step pattern.

The sample, used in acquiring the data shown in Fig. 7, was fine silica sand with 0.2% by weight of water with 100 mM of KCL. The measured resistance was 273.9 kohms where the $E_{con} = 10$ mV.

For this value of E_{con} the maximum current through the sample is ± 100 nA (see Eq. 2). Notice that this current is not symmetrical with respect to zero current. This is typical for electrical chemical cells where offset voltages are present. The resistance of the sample was determined from a least squares fit to the 400 data points seen in Fig. 7b.

In developing the methodology for these measurements, the choice of E_{con} is critical. As discussed above, the value for E_{con} must be such that the experimental data falls within the red dashed area seen in Fig. 6.

In addition, to this equipment limit, soil samples were found to exhibit a breakdown characteristic especially at low moisture content or at low temperatures. A typical response is seen in Fig. 8. Here it is seen that as higher currents are forced through the sample, the voltage and current change abruptly. From a circuit stand point, the sand samples no longer exhibit linear current-voltage characteristics. Our thoughts on the physical nature, of this very interesting phenomena, are presented in the Discussion Section.

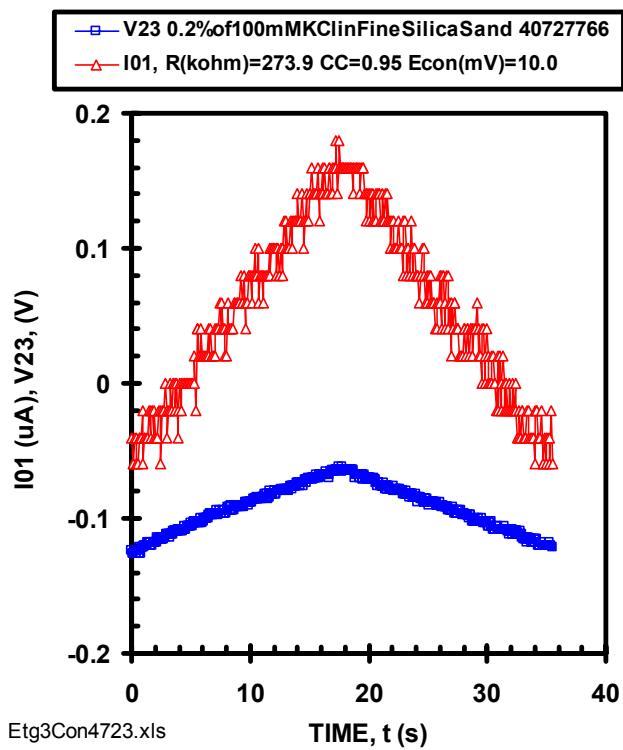


Figure 7a. Time dependent current-voltage characteristics.

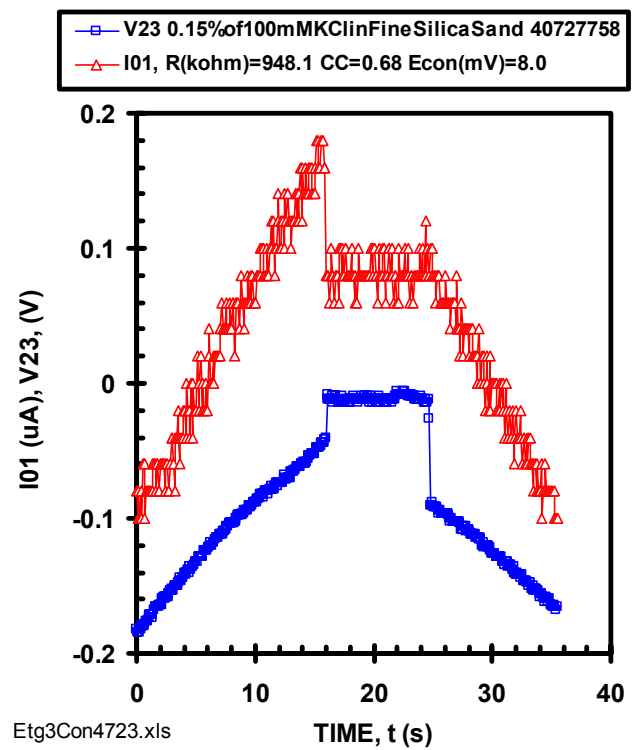


Figure 8a. Time dependent current-voltage characteristics showing breakdown phenomena.

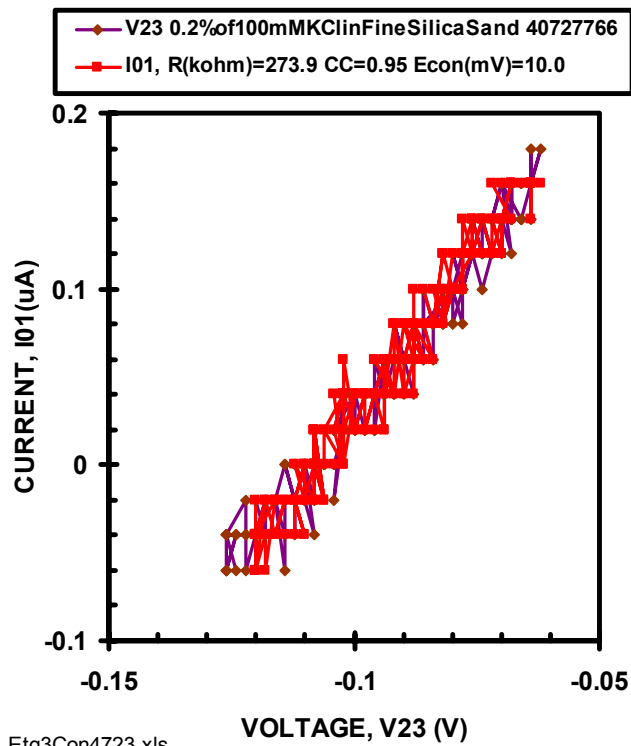


Figure 7b. Current versus voltage with linear characteristics

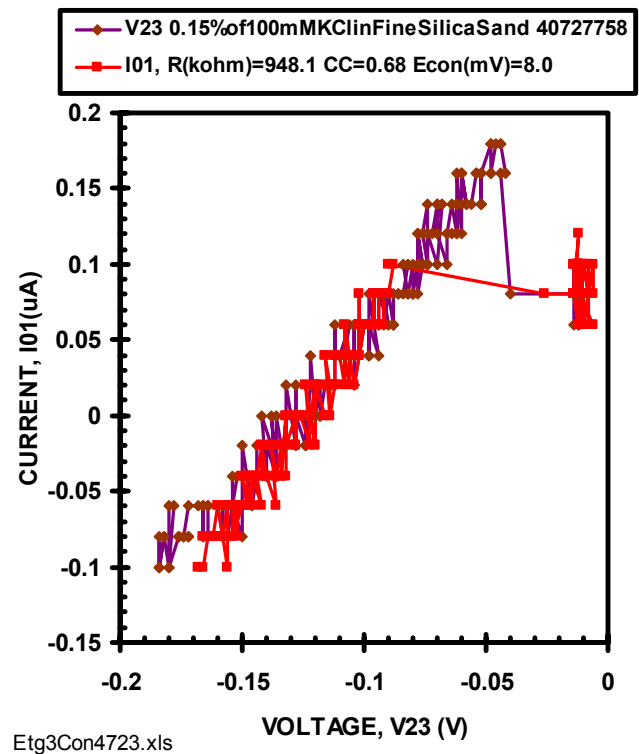


Figure 8b. Current-voltage characteristic showing breakdown phenomena.

3.2 Correlation Coefficient Analysis

In order to facilitate data acquisition, software was developed to allow the acquisition of current-voltage curves at different values of E_{con} ; hence, different values of maximum current. The procedure is illustrated in Fig. 9 which shows that E_{con} is stepped through eight values from 2 mV to 32 mV.

As mentioned, the resistance was derived by fitting the current-voltage characteristics and the associated correlation coefficient, CC, was determined. This procedure allowed a quick identification of measurements that were having problems due either to equipment limitations (red dashed bound line in Fig. 6) or sample breakdown.

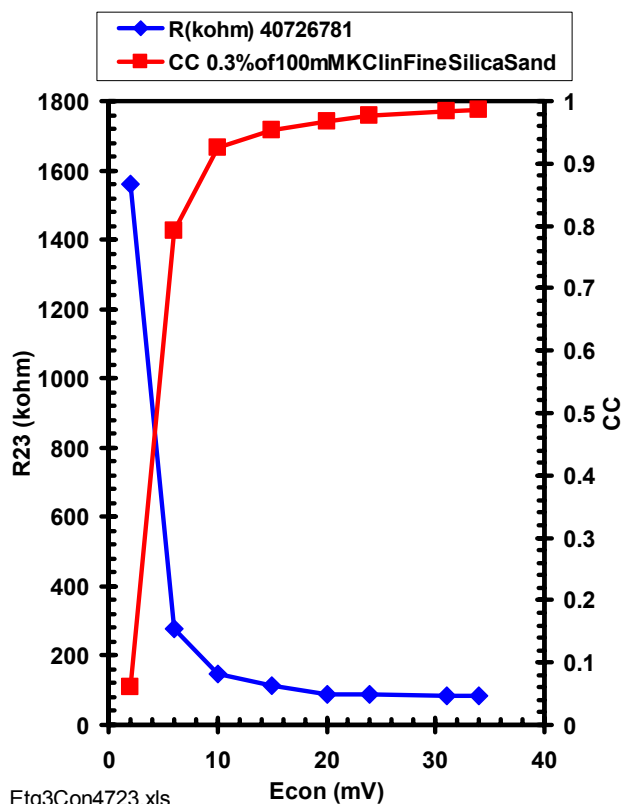


Figure 9. Finding acceptable R_{23} values depends on finding E_{con} values with CC (correlation coefficients) above 0.9.

3.3 Graphical User Interface

A graphical user interface (GUI), seen in Fig. 10, was developed to allow users to specify the type and parameters for measuring the conductivity sensor. The *Type of Experiment* is selected through the combo box interface showing *Conductivity*. The experiment parameters are defined in the *Setup* window including the voltage limits (E_1 and E_2), scan rate (S), deposition time ($T_{dep} = 0$), number of samples/slope (N_p) and average ($N_a = 200$) points/sample. The interface also specifies that the REDOX cells are biased in Galvanostat mode allowing no current to flow from these cells. The *ADC Prog. window* is used to put those cells in a neutral (zero current) electrochemical state. The *DAC Prog. window* is used to selected the cells to

receive the DAC ramp signal. The *Switch Prog.* window is used to select potentiostat or galvanostat mode.

Once the experiment is started, the GUI shows the *Status* of the experiment and the execution time. This information is important since some experiments can take several hours. GUI also allows the user to perform eight experiments automatically each with a different E_{con} . The number of experiments and E_{con} parameters for each experiment are defined in the *Exp. Series: Tdep* window. The interface also allows the user to monitor results through the *Results* window while the experiments are running.

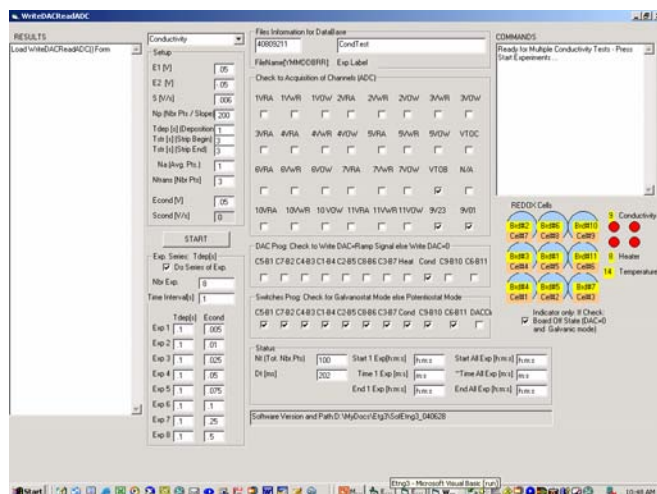


Figure 10. Conductivity GUI.

3.4 Electrode Cleaning Procedure

Before measuring contaminated water, the electrodes are cleaned. During the past six months a number of cleaning procedures were tried. Our latest procedure is as follows. First the raw ceramic substrate is lightly lapped with 2000 grit silicon carbide paper to remove any hillocks remaining after the electrode screen printing process. After an ASV measurement sequence, residual metals are removed from the electrodes using a finishing pad available from 3M (Part 7414). Residue from this process is removed using a cotton swab soaked in a flux remover available from M. G. Chemicals Part 414. The ceramic is given a final cleaning using a cotton swab soaked in IPA (IsoPropyl Alcohol). The residual IPA is removed using a dry cotton swab. If sterility is needed, the ceramic substrate, polycarbonate chamber and O-ring can be autoclaved.

4 EXPERIMENTAL RESULTS

A number of sand samples were used in the following experiments. They were first characterized and then measured in the E-Tongue-3 apparatus with the soil chamber shown in Fig. 1a.

4.1 Sand Sizing

The sands were characterized using photomicroscopy and analyzed using a software program which characterized the

size the particles. The results in Fig. 11a are for fine silica sand, the results in Fig. 11b are for coarse silica sand, and the results Fig. 11c are for Moses Lake basalt. The photomicroscope image software revealed the angularity and mean dimension for the particles. As seen from Figure 11, the particles were in the 100 to 200 μm range.



Figure 11a. Fine Silica Sand Mean d: 107 μm



Figure 11b. Coarse Silica Sand Mean d: 208 μm

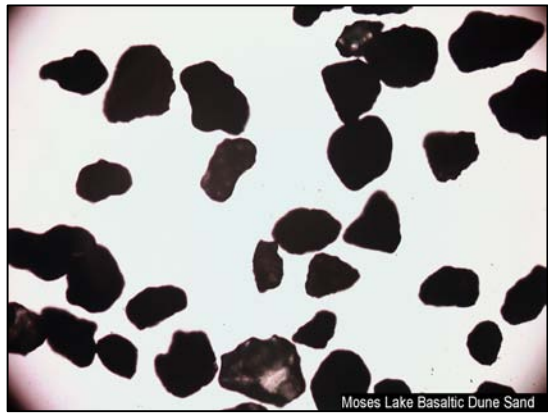


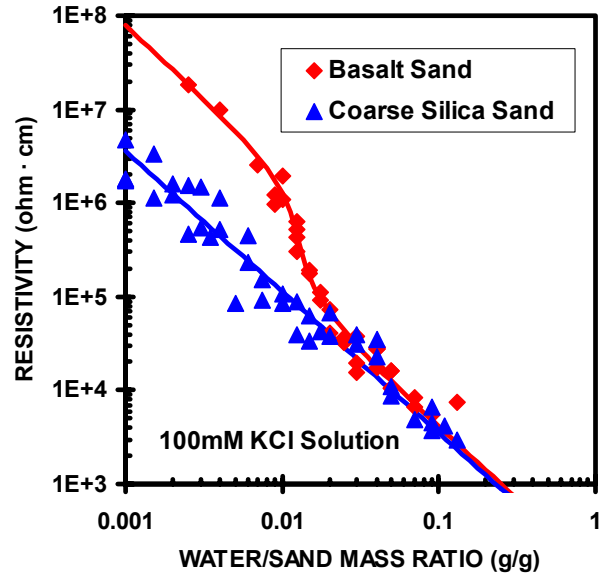
Figure 11c. Basalt Mean d: 152 μm

4.2 Sand Resistivity

The data shown in the following figures were obtained by first weighing 10.0 g of sand. Then a fraction of pure water doped with 100 mM KCl was introduced into the sand using a pipette with 0.1 mL resolution. The sand and water were mixed by shaking until the sample was uniform. Then the

mixture was introduced into the sample chamber shown in Fig. 1a. The mixture was pressed into place using a cylinder that was rotated so as to compact the sample as much as possible thus removing residual air. The cylinder was left in place during the experiment in an attempt to seal the sample to minimize moisture evaporation during the data acquisition period.

Results for coarse silica sand and basalt sand are shown in Fig. 12. The data show that measurements were acquired over the moisture range from 0.1% to 15% by weight.



UNR2004Matrix40803Final.xls

Figure 12. Resistivity of two types of moist sand measured at room temperature.

The data in Fig. 12 were fitted to the following equation

$$\log\left(\frac{\rho}{\rho_0}\right) = \log\left(\frac{M}{M_0}\right)^{a_0} + \frac{\log\left(\frac{M}{M_0}\right)^{a_1}}{1 + \log\left(\frac{M}{M_0}\right)^{a_2}} \quad (7)$$

where M is the mass ratio representing mass ratio values given on the horizontal axis of Fig. 12. The coefficients of Eq. 7 are a_0 , a_1 , and a_2 . A fit by eye to the data in Fig. 12 yields the parameters listed in Table 1.

Table 1. Fitting Parameters for Eq. 7

	Coarse Silica Sand	Basalt Sand
$\log M_0$	-1.9	-1.9
a_0	-1.5	-1.5
a_1	0	-7.0
a_2	0	+10
$\log \rho_0$	+5.6	+4.9

Coarse silica sand dependence as seen in Fig. 12 is similar to that observed by Archie [6]. Archie's law relates the resistivity of moist sand to porosity expressed as a fraction for unit volume rock. The data in Fig. 12 was acquired as a

mass fraction of water to sand. Despite this difference, values for a_0 from the literature [7] range from -1.37 to -1.95. These values are comparable with $a_0 = -1.5$ found in these studies.

The basalt sand dependence in Fig. 12 shows a transition from wet behavior at high water content to dry behavior at low water content. The slope of the curves is the same for both basalt sand and coarse silica sand.

The same procedure used to prepare the samples at room temperature was used to measure samples as a function of temperature. The results are shown in Fig. 13 for the coarse silica sand sample. In addition to the sand measurements, water measurements were also acquired. At each temperature the system was allowed to equilibrate for 15 minutes before taking data. At temperature below 0 °C the breakdown phenomena shown in Fig. 8 was also observed. For these cases, E_{con} values were reduced to avoid the breakdown phenomena.

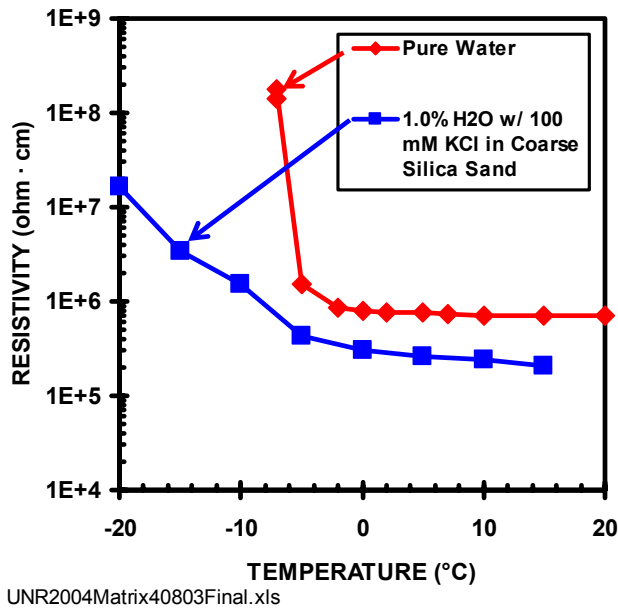


Figure 13. Temperature dependence of coarse silica sand with 1% H₂O and doped with 100mM HCl and pure water.

These results in Fig. 13 show an increase in the resistivity of the mixture as the temperature is decreased below 0 °C. The resistivity behavior of the water and sand with temperature are similar to those noted by Scott [8]. They too observed a large increase in resistivity with decreasing temperature. Also they observed an increase in resistivity at temperatures a few degrees less than 0 °C.

5 DATA ANALYSIS

The conduction of electricity in moist soils has been described by Rhoades [9]. He indicated that conduction occurs by several mechanisms. The soil conduction paths are depicted in Fig. 14 where the numbered paths correspond to the follow mechanisms:

- (1) **Particle conduction:** Consists of conduction through certain conducting minerals [7].
- (2) **Electrolyte (solution) conduction:** Consists of conduction through the water electrolyte which depends on the concentration and mobility of cations and anions in solution [10].
- (3) **Mixed conduction:** Consists of conduction through conducting minerals and through the electrolyte.
- (4) **Surface conduction:** Consists of conduction through water adsorbed on particle surfaces.

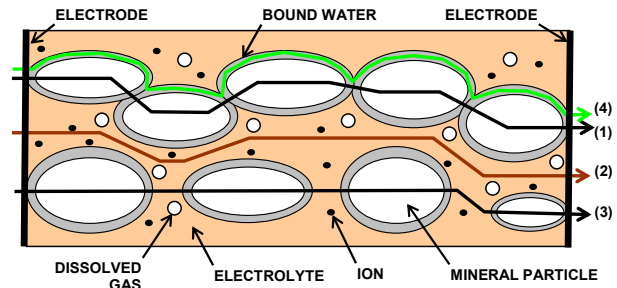


Figure 14. Model of conduction paths in moist soils.

This model is used to explain the observations in Fig. 12. First, the particles used in this study are insulators that eliminate paths #1 and #3 from consideration. For high water content, path #2 is a viable explanation; this path has a low resistance to flow of current through the electrolyte. For low water content, path #4 is viable for this path will have a high resistance to the flow of current. For the basalt sand, there is a clear transition from one conduction mode to the other but for the coarse silica sand there appears to be no transition between conduction modes. The breakdown phenomena observed in Fig. 8 appears to be due to a rupture of the current path. Reasons for the transition behavior for the basalt and the breakdown phenomena are being sought.

The authors could not fine a model for the behavior of soils at temperature below 0 °C. This appears to be a frutfull area for research.

6 CONCLUSION

Results presented here shown that electrical conductivity techniques are viable in characterizing soils with as little as 0.1% water. Such a low percentage of water is less than the projections for the driest soils on Mars. The technique can be used when the temperature drops below 0 °C. In this study measurements were used to characterize soils at temperature as low as -20 0 °C. The results for soils measured at room temperature are consistent with Archie's Law in that the slope of the log resistivity versus log soil moisture percentage has a slope of -1.5.

7 APPENDIX: Conductivity Sensor Calibration

The geometrical factor was determined for the conductivity sensor shown in Fig. 3 where the electrodes are discs not

points. The disc geometrical factor, G_d , was determined using solutions of HCl where the ionic conductivity is well known.

The resistance values, R_{23} , shown in Fig. A1, were measured using various HCl solutions. These measurements were acquired where the sample thickness is large compared to the probe spacing so the sample is considered to be infinitely thick. Recall that the probe spacing for the conductivity sensor is $s = 0.125$ cm.

A simple model was developed to fit the results seen in Fig. A1. The model consists of two parallel resistors one resistor represents the undoped water resistance, R_0 , and the other resistor represents the electrolyte resistance, R_e . The total resistance is the parallel combination of R_0 and R_e :

$$R_{23} = \frac{R_0}{1 + \frac{R_0}{R_e}} \quad (\text{A1})$$

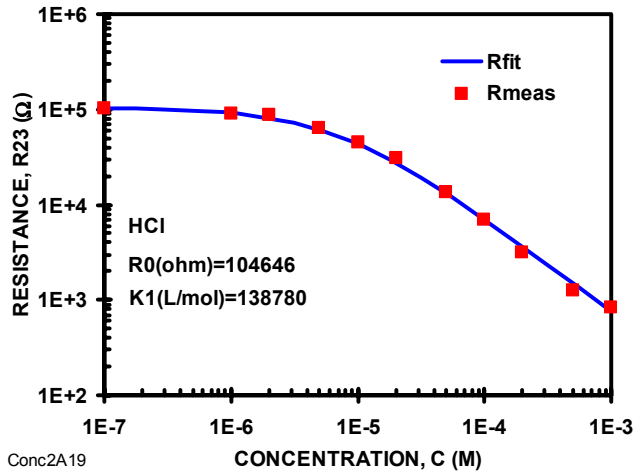


Figure A1. Conductivity sensor HCl response.

The resistance of the electrolyte is given by:

$$R_e = \rho_e / (G_d \cdot s) \quad (\text{A2})$$

and the resistivity of the electrolyte is [10]:

$$\rho_e = 1000 / (\lambda \cdot C) \quad (\text{A3})$$

where λ is the electrolyte ionic conductivity with units of $\text{cm}^2/(\Omega \cdot \text{mol})$, and C is concentration of ions in solution with units of mol/L or M. The conversion factor 1000 has units of cm^3/L . The combination of the above two equations yields a second equation for the electrolyte resistance:

$$R_e = 1000 / (G_d \cdot s \cdot \lambda \cdot C) \quad (\text{A4})$$

Combining this equation with Eq. A1 yields:

$$R_{23} = \frac{R_0}{1 + \left(\frac{R_0 \cdot \lambda \cdot G_d \cdot s}{1000} \right) C} \quad (\text{A5})$$

This equation was used to fit the data shown in Fig. A1. The fitting equation was obtained by rearranging the above equation to form the following linear equation:

$$R_{23} = [R_0] + [-K_1] \cdot R_{23} \cdot C \quad (\text{A6})$$

where the coefficient:

$$K_1 = (R_0 \cdot G_d \cdot s \cdot \lambda) / 1000 \quad (\text{A7})$$

The result of a least squares fit to the data shown in Fig. A1 is $R_0 = 104.6$ k Ω and $K_1 = 136,780$ (L/mol). The disc geometrical factor, G_d , is calculated from Eq. A6 as:

$$G_d = K_1 \cdot 1000 / (R_0 \cdot s \cdot \lambda) \quad (\text{A8})$$

where the conductivity of HCl for infinite dilution is $\lambda = 425.96$ $\text{cm}^2/(\Omega \cdot \text{mol})$ [11]. Introducing appropriate values for the parameters in Eq. A8 leads to the value for the disc geometrical factor, $G_d = 24.9$ which is unitless. This value is used to calculate the resistivity of the data shown in Figs. 12 and 13:

$$\rho_\infty (\Omega \cdot \text{cm}) = G_d \cdot s(\text{cm}) \cdot R_{23}(\Omega) = 3.11 \cdot R_{23}(\Omega) \quad (\text{A9})$$

8 ACKNOWLEDGMENTS

The work described in this paper was performed by the Jet Propulsion Laboratory, California Institute of Technology, under a contract with the National Aeronautics and Space Administration. The overall effort is supported by an ASTID02 entitled “An instrument for detecting water, brines and signatures of microbial activity on Mars and Europa”. The authors are indebted efforts of Dennis Martin, President, Halcyon Microelectronics, Inc. Irwindale, CA for the fabricating the new E-Tongue 3 chambers. One author, Buehler, is in indebted to Prof. Jesse Adams and Ben Rogers of Univ. Nevada, Reno for sending two excellent summer students, Tommy Sant and Ethan Brizendine, to JPL during the summer of 2004. File: AeroWaterPub5112.doc.

9 REFERENCES

- [1] W. V. Boynton, et.al. “Distribution of Hydrogen in the Near Surface of Mars: Evidence for Subsurface Ice Deposits”, Science, 297, 81 92002.
- [2] I. G. Mitrofanov, et.al., “CO₂ Snow Depth and Subsurface Water-Ice Abundance in the Northern Hemisphere of Mars”, Science, 300, 2081 (2003).

[3a] G. M. Kuhlman, D. Keymeulen, and M. G. Buehler, and S. P. Kounaves, "Detecting Heavy Metals in Solution Using Electronic-Tongue 3 REDOX Water Quality Sensors", 2004 IEEE Aerospace Conference, *Vol. 1, Cat. No. 0-7803-8155-6/04*

[3b] M. G. Buehler, G. M. Kuhlman, N. V. Myung, D. Keymeulen, S. P. Kounaves, D. K. Newman and D. Lies, "Planar Array REDOX Cells and pH Sensors for ISS Water Quality and Microbe Detection", International Conference on Environmental Systems, (July 2003) paper 03ICES-216.

[4] M. G. Buehler and W. R. Thurber, "A Planar Four-Probe Test Structure for Measuring Bulk Resistivity," IEEE Trans. On Electron Devices, Vol. ED-23, pp. 968-974.1976.

[5] M. Buehler, G. Kuhlman, D. Keymeulen, N. Myung, and S. Kounaves, "Planar REDOX and Conductivity Sensors for ISS Water Quality Measurements", Aerospace Conference, 2003. Proceedings. 2003 IEEE, Volume: 2, March 8-15, 2003, pages 2_527 – 2_533

[6] G. E. Archie, "The electrical resistivity log as an aid in determining some reservoir characteristics, Trans. Am. Inst. Min. Eng., 146, 54, 1942.

[7] R. S. Carmichael, *Practical Handbook of Physical Properties of Rocks and Minerals*, CRC Press (Boca Raton, Florida, 1990)

[8] Scott, W.J., Sellmann, P.V, and Hunter, J.A, 1990, "Geophysics in the study of permafrost", in Geotechnical and Environmental Geophysics, Vol 1. Ed. S.H.Ward, SEG

[9] J. D. Rhoades, P.A.C. Raats, and Prather, R.J., 1976, "Effects of liquid-phase electrical conductivity, water content, and surface conductivity on bulk soil electrical conductivity." Soil Sci. Soc. Am. J. 40, 651-655.

[10] A. J. Bard and L. R. Faulkner, *Electrochemical Methods*, 2nd Edition, Wiley & Sons (New York, 2001).

[11] Handbook of Chemistry and Physics, Electrochemical Series, No. 74, CRC Press (Boca Raton, 1994), p. 5-87

10 BIOGRAPHIES



Martin G. Buehler received the BSEE and MSEE from Duke University in 1961 and 1963, respectively and the Ph.D. in EE from Stanford University in 1966 specializing in Solid State Electronics under G. L. Pearson and W. Shockley. He worked at Texas

Instruments for six years, at National Bureau of Standards (now NIST) for eight years, and since 1981 has been at the Jet Propulsion Laboratory where he is a Senior Research Scientist. At JPL he has developed p-FET radiation monitors for CRRES, Clementine, TELSTAR and STRV, E-nose which flew on STS-95 with John Glenn, an electrometer for the Mars '01 robot arm, and E-Tongue for ISS water quality. Currently, he serves on the staff of the New Millennium Program as a technical analyst. Martin is a Life Member of the IEEE, and a member of Tau Beta Pi, and Sigma Nu. He holds 16 patents and has published over one hundred papers.

Thomas A. Sant is majoring in mechanical engineering at the University of Nevada, Reno with a projected graduation



date of May 2006. He has been a member of the Nanomechanics Research Group at UNR since his year freshman year, 2002. His experience with the research group has lead to him being named co-author of an *Applied Physics Letters* publication on microcantilever

chemical detection, his direct support in the development of UNR's Nanofabrication Facility, and the opportunity to work with an excellent group of engineers and scientists at JPL. Thomas is an active member of the ASME.

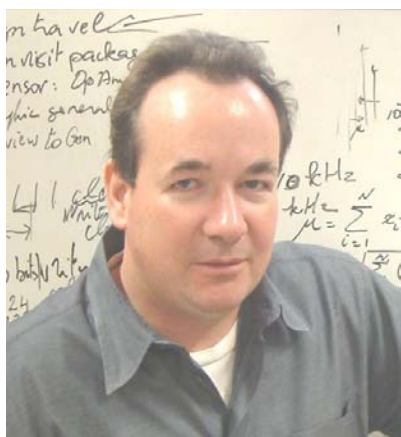
Ethan Brizendine is a junior at the University of Nevada Reno, where he is currently pursuing a Bachelor's degree in Mechanical Engineering. He has worked at the Nevada



Terawatt Facility's nanotechnology laboratory for the past year, where he acquired a fascination in the many applications of nanotechnology.

During the summer of 2004, he worked at the Jet Propulsion Laboratory under the supervision of Dr. Martin Buehler,

where he researched and tested electric sensors which may be able to detect the water content of the Martian surface.



Didier Keymeulen received the BSEE, MSEE and Ph.D. in Electrical Engineering and Computer Science from the Free University of Brussels, Belgium in 1994. In 1995 he was the Belgium laureate of the Japan Society for the Promotion of Science Post

Doctoral Fellowship for Foreign Researchers. In 1996 he joined the computer science division of the Japanese National Electrotechnical Laboratory as senior researcher. Since 1998, he is member of the technical staff of JPL in the Bio-Inspired Technologies Group. At JPL, he is responsible for the applications of the DoD and NASA projects on evolvable hardware for adaptive computing that leads to the development of fault-tolerant electronics and autonomous and adaptive sensor technology. He served as the chair, co-chair, program-chair of the NASA/DoD Conference on Evolvable Hardware. Didier is a member of the IEEE.



Gregory M. Kuhlman: Greg received a B.S. degree in Bacteriology from the University of Wisconsin-Madison in 1995. Following graduation Greg has worked for the University of Wisconsin-Madison, Covance Laboratories Incorporated, and Amgen Incorporated before coming to the Jet Propulsion Laboratory (JPL) in 2000. Greg's skills include classical bacteriology techniques, modern molecular biology techniques and extensive protein chemistry skills. Greg

has mastered most modern chromatographic techniques such as High Pressure Liquid Chromatography (HPLC), Fast Protein Liquid Chromatography (FPLC) and Capillary Zone Electrophoresis (CZE). As an undergraduate at the University of Wisconsin-Madison Greg worked in the lab of Dr. Eric Johnson, world renown researcher of clostridium botulinum and other food borne pathogens, and has acquired the skills for working with pathogenic microorganisms. At JPL Greg focuses his time between two groups. He works with the Planetary Protection Technologies Group where he

is researching and evaluating advanced technologies for molecular detection of microbes on spacecraft materials and in spacecraft assembly facilities. Greg also works with the Microdevices Laboratory where he is utilizing his biology skill set to test and study the effects of biofilms on space flight hardware.



Marcel G. Schaap received a BA in Chemistry (1984) and a MS (1990) and PhD (1996) in Soil Chemistry and Soil Physics from the University of Amsterdam, the Netherlands, specializing in the measurement and modeling of soil water contents and soil electric

conduction. In 1996 he joined UC Riverside and, through a collaborative agreement, the George E. Brown, Jr. Salinity Laboratory, where he developed artificial neural network based software for the estimation of soil hydraulic properties. His current interests are the measurement and modeling of soil dielectric properties, development of high-precision automated soil hydraulic measurements, and the modeling of micro-scale fluid flow and interfacial phenomena with Lattice Boltzmann Models. He has published over 30 peer-reviewed papers on soil and environmental chemistry and physics.



Suresh Seshadri received a B.S. from Columbia University and a Ph.D. from Yale University, both in Electrical Engineering. A senior member of technical staff at the Jet Propulsion Laboratory since 2000, he is currently Principal Investigator

on projects to develop (1) a CMOS APS imager in Silicon-On-Insulator (SOI) technology and (2) an electrical & electrochemical sensor suite to detect water and biosignatures on Mars. Prior work on CMOS image sensors at JPL culminated in the demonstration of a computational difference imager. He has also investigated radiation hardness characteristics of CMOS imagers. From 1999-2000, he led the SiC power device development effort (diodes, thyristors, & MOSFETs) at Northrop Grumman Corporation, Electronic Sensors and Systems Division, which he joined in 1996. Highlights of those efforts include demonstration of the first motor control circuit using all-SiC

power switching devices. His work as a member of technical staff at the Westinghouse Science & Technology Center from 1995-1996 earned him a Westinghouse Signature Award of Excellence for his contribution to the first demonstration of operational SiC neutron detectors after exposure to neutron fluences typical in a nuclear reactor environment. He is the author or co-author of over 20 technical papers.



Robert C. Anderson

received his Bachelor Science Degree in geology in 1979 and in 1979 received the Master of Science from Old Dominion University in geology with emphasis on structural geology and mapping tectonic features surrounding the Tharsis region of Mars. In 1995, he received a Doctor of Philosophy from the

University of Pittsburgh in geology with emphasis on visible and near-infrared remote sensing. His Ph.D. research was centered on mapping young Quaternary surfaces, desert pavements and varnish, and soils around the Whipple Mountains of southwestern Arizona to better understand the past climatic history of the region. Bob joined JPL in 1996 where he has contributed to the Mars Pathfinder Project as the science coordinator of the Mineralogy and Geochemistry Science Operations Group. Next he was he was Deputy Director of Mars Education and then Mission Planner for the Mars 2001 lander. His current science research is centered on unraveling the geologic history of Mars with emphasis on understanding the tectonic, structural, paleohydrologic evolution of the Tharsis region. He is a Senior member of the Technical Staff at JPL and is currently employed as the Investigation Scientist for the Rock Abrasion Tool (RAT), Soil properties, and science support for Mission Operations on the Mars 03 mission. He is presently Adjunct Research Faculty at the University of Pittsburgh Department of Geology and Planetary Science as well as Adjunct Faculty at Pasadena City College where he is presently teaching a class on Planetary Geology.